

## **V(z) f-k modelling and resolution simulation**

Gary F. Margrave

### **ABSTRACT**

This paper combines several previous research results to create displays that illustrate the advantage of using  $v(z)$  simulations (instead of constant velocity) for acquisition design. First, the  $v(z)$  migration theory, based on nonstationary filters, is summarized. Then, nonstationary inverse filter theory is used to create a  $v(z)$  modelling theory by inverting the migration theory. For discrete data, the  $v(z)$  migration is accomplished by a matrix multiplication in the Fourier domain. Each wavenumber of the f-k spectrum of the data is multiplied by a matrix  $M$  which applies the nonstationary migration filter. The nonstationary modelling filter is a matrix  $M^*$  that is the conjugate-transpose (adjoint) of the migration filter. The operator product  $MM^*$  is very nearly unity. Numerical simulations show that  $v(z)$  f-k modelling produces high quality results with far fewer Fourier wrap-around artifacts than constant velocity modelling. When a modelled response is truncated in space and time (to simulate finite aperture and record length) and then migrated, the result shows the expected geometric artifacts of limited resolution. Resolution simulations with  $v(z)$  produce substantially smaller estimates of the minimum resolvable size than do constant velocity simulations. Acquisition designs to specific resolution requirements are less expensive when done with  $v(z)$  theory instead of constant-velocity theory.

### **INTRODUCTION**

There are a great many factors to be considered in designing a seismic acquisition geometry such as source and receiver intervals, fold, survey aperture, record length, source-receiver azimuth, etc. The complexity of the problem means that detailed and realistic predictions are best done with numerical simulations that approximately model wave propagation and acquisition sampling. Usually such simulations are done with constant velocity assumptions because the simulation algorithms are simpler and, it is often believed, greater realism is not necessary in design. However, the ultimate purpose of this paper is to demonstrate that a design which models the vertical variation of velocity leads to dramatically different resolution predictions than the constant-velocity simulations. The details of aperture, record length and sampling limitations for  $v(z)$  have been presented elsewhere (e.g. Margrave [1997a and 1997b]). The purpose of this paper is to use  $v(z)$  modelling and migration to create example simulations illustrating the basic concepts.

The paper begins with the construction of a new  $v(z)$  modelling method that is the conjugate operation to  $v(z)$  f-k migration introduced by Margrave (1998). This derivation is an interesting exercise in the inversion of nonstationary filters and leads to the result that the modelling operator is the conjugate transpose (adjoint) of the migration operator in the Fourier domain. Once the theory is developed, it is used,

together with  $v(z)$  f-k migration, to conduct example resolution simulations that demonstrate the main point of the paper (as discussed above).

### DERIVATION OF F-K MODELLING

The conventional way to derive a wave-theory modelling algorithm is to set up the appropriate wave equation and initial conditions and then develop a solution from these first principles. There are many examples of such an approach in the literature and there is no need to repeat it here. Instead, this derivation starts with the theory of f-k migration for  $v(z)$  media (as developed in Margrave [1998]) where the final migration was expressed as a nonstationary filter operation applied to the data. Then, a modelling algorithm is developed by applying the concept of nonstationary inverse filtering to the migration formulae. The result is the well-known WKBJ method that can be found in textbooks such as Grant and West (1965) or Aki and Richards (1980). This approach demonstrates the utility of nonstationary inverse filtering and emphasizes the inverse relationship between migration and modelling.

#### Restatement of the $v(z)$ f-k migration algorithm

The simplest concept of Fourier domain modelling is a simple extension of the exploding reflector concept (Lowenthal et al., 1976). That is, assume an arbitrary spatial  $(x,z)$  distribution of reflectivity embedded in a medium where the wave propagation speed depends only on  $z$ ,  $v(z)$ . In this context, Margrave (1998) showed that f-k migration can be written as a nonstationary filtering operation. This operation, called  $v(z)$  f-k migration, was cast as a direct parallel to Stolt's (1978) constant velocity f-k migration. As such, it computes the migrated f-k spectrum directly from the unmigrated f-k spectrum by

$$\theta(k_x, \xi) = \frac{1}{2\pi} \int_{-\infty}^{\infty} \varphi(k_x, \omega) M(k_x, \xi, \omega) d\omega \quad (1)$$

where  $\varphi(k_x, \omega)$  is the 2-D Fourier transform (f-k) of the recorded seismic data,  $\theta(k_x, \xi)$  is the 2-D Fourier transform of the migrated image, and  $M(k_x, \xi, \omega)$  is the nonstationary *migration filter*. The migration filter is computed by

$$M(k_x, \xi, \omega) = \int_{-\infty}^{\infty} m(k_x, \tau, \omega) \exp(-i\xi\tau) d\tau \quad (2)$$

where  $m(k_x, \tau, \omega)$  is known analytically from WKBJ wave theory (Grant and West, 1965, Aki and Richards, 1980) as

$$m(k_x, \tau, \omega) = \exp\left(i\omega \int_0^{\tau} \sqrt{1 - p^2 v^2(u)} du\right) \quad (3)$$

where  $p=k_x/\omega$  is the horizontal slowness or ray parameter, and  $v$  is the vertical velocity variation as a function of vertical travelttime.

### **Inverting f-k migration to get f-k modelling**

The construction of a WKBJ modelling algorithm is essentially a matter of inverting equation (1) to solve for  $\varphi(k_x, \omega)$  given  $\theta(k_x, \xi)$ . This style of integral equation is known in the mathematical literature as a Fredholm equation of the first kind (Riley et al., 1997). Such equations are difficult to solve exactly for general kernels (M is the kernel in this case). However, when M has the property known as “translation invariance” (i.e  $M=M(k_x, \xi-\omega)$ ) then equation (1) is the prescription of a stationary filter and the well-developed inverse techniques of Wiener filter theory apply.

Margrave (1997) and Margrave and Ferguson (1998) gave a simple algorithm for constructing an approximate inverse to equation (1). This method reduces to an exact stationary inverse if translation invariance holds and gives a very accurate approximation if M shows slow variation with translation (i.e. it is slightly nonstationary). To illustrate the method in its simplest terms, it is useful to use nonstationary filter theory to rewrite equation (1) as a mixed-domain expression. That is

$$\psi(k_x, \tau) = \frac{1}{2\pi} \int_{-\infty}^{\infty} \varphi(k_x, \omega) \alpha(k_x, \tau, \omega) \exp(i\omega\tau) d\omega \quad (4)$$

where  $\psi(k_x, \tau)$  is the inverse Fourier transform (from  $\xi$  to  $\tau$ ) of  $\theta(k_x, \xi)$  and  $\alpha(k_x, \tau, \omega)$  is given by

$$\alpha(k_x, \tau, \omega) = m(k_x, \tau, \omega) \exp(-i\omega\tau). \quad (5)$$

This rewrite may seem a bit contrived because of the exponential factors that cancel when equation (5) is inserted in equation (4); however, it is instructive to continue with this form as it closely reveals the connection with stationary inverse filtering.

Equation (4) applies the nonstationary filter,  $\alpha(k_x, \tau, \omega)$ , using the mixed-domain form known as nonstationary combination. (The phrase “mixed-domain” means that the signal [ $\varphi(k_x, \omega)$ ] changes domain from  $\omega$  to  $\tau$  as the filter is applied.) Its approximate inversion is accomplished by applying  $\alpha^{-1}(k_x, \tau, \omega)$  as a nonstationary convolution, again in mixed domain form. Thus

$$\varphi(k_x, \omega) = \int_{-\infty}^{\infty} \psi(k_x, \tau) \alpha^{-1}(k_x, \tau, \omega) \exp(-i\omega\tau) d\tau \quad (6)$$

should give an excellent approximation to the inverse of equation (4). Substitution of equation (4) into equation (6) shows why this is so:

$$\varphi(k_x, \omega) = \int_{-\infty}^{\infty} \varphi(k_x, \omega') \Delta(\omega, \omega') d\omega \quad (7)$$

where

$$\Delta(\omega, \omega') = \frac{1}{2\pi} \int_{-\infty}^{\infty} \alpha^{-1}(k_x, \tau, \omega) \alpha(k_x, \tau, \omega') d\tau = \frac{1}{2\pi} \int_{-\infty}^{\infty} m^{-1}(k_x, \tau, \omega) m(k_x, \tau, \omega') d\tau. \quad (8)$$

Thus equation (6) inverts equation (4) if  $\Delta(\omega, \omega')$  reduces to  $\delta(\omega - \omega')$ . In the present context, this is exactly true if  $v$  is constant and is approximately so unless  $v$  varies extremely rapidly.

Practical considerations dictate that  $m(k_x, \tau, \omega)$ , as given by equation (3) should only be inverted if  $m$  is oscillatory. That is, if  $p^2 v^2(u) > 1$ , decaying exponential behavior should be enforced in both  $m$  and  $m^{-1}$ . (Physically, decaying exponentials are the expected behavior in forward modelling and their inversion in migration would require a growing exponential.) These considerations are accommodated if  $m^*$  (the complex conjugate of  $m$ ) is used in place of  $m^{-1}$  in equation (8). With these considerations, equation (6) becomes

$$\varphi(k_x, \omega) = \int_{-\infty}^{\infty} \psi(k_x, \tau) m^*(k_x, \tau, \omega) d\tau. \quad (9)$$

A complete counterpart to equation (1) can now be developed by moving equation (9) fully into the Fourier domain. This is accomplished by replacing  $\psi(k_x, \tau)$  with the inverse Fourier transform of its spectrum. This gives

$$\varphi(k_x, \omega) = \int_{-\infty}^{\infty} \left[ \frac{1}{2\pi} \int_{-\infty}^{\infty} \theta(k_x, \xi) \exp(i\xi\tau) d\xi \right] m^*(k_x, \tau, \omega) d\tau. \quad (10)$$

Interchanging the order of integration in equation (10) leads to

$$\varphi(k_x, \omega) = \frac{1}{2\pi} \int_{-\infty}^{\infty} \theta(k_x, \xi) M^*(k_x, \xi, \omega) d\xi \quad (11)$$

where the nonstationary modelling filter,  $M^*$ , is given by

$$M^*(k_x, \xi, \omega) = \int_{-\infty}^{\infty} m^*(k_x, \tau, \omega) \exp(i\xi\tau) d\tau = \left( \int_{-\infty}^{\infty} m(k_x, \tau, \omega) \exp(-i\xi\tau) d\tau \right)^*. \quad (12)$$

Comparison of equation (12) with equation (2) shows that  $M^*$  is just the complex conjugate of  $M$ .

Equation (11) creates the spectrum of zero offset seismic data directly from the spectrum of the geologic model. In comparison with the inverse operation expressed by equation (1), equation (11) uses the conjugate integral kernel but also the integration is over  $\xi$  in equation (11) and over  $\omega$  in equation (1). In a numerical implementation, these integral expressions become matrix-vector multiplications where the matrices representing  $M^*$  and  $M$  are conjugate transposes of one another.

## EXAMPLES OF MIGRATION AND MODELLING FILTERS

Figures 1 and 2 show examples of the migration filter,  $M$ , and the modelling filter,  $M^*$ , for the specific case of constant velocity. These figures display only the magnitude of the filters so, though they are clearly transposes of one another, the complex conjugation is not evident. Both filters show energy maximized along a hyperbolic track which satisfies  $\xi^2 - \omega^2 = k_x^2 v^2$  (see Margrave [1998] for an explanation). In the infinite aperture, analytic case, these are Dirac delta function singularities that implement the exact one-to-one mapping between migrated and unmigrated frequencies or the reverse. In this discrete case, each row of each filter contains an optimal sinc function interpolator that accomplishes the required spectral interpolation.

Figures 3 and 4 show the magnitudes of  $M$  and  $M^*$  for the case of a velocity function that increases linearly with depth, or equivalently, exponentially with vertical travelttime. The matrices are no longer singular but instead show energy spread between hyperbolae defined by the minimum and maximum velocities.

Figures 5 and 6 show the magnitudes of  $M$  and  $M^*$  for a case when the velocity model consists of three constant velocity layers. Each layer causes a distinct hyperbolic track in the filters.

According to the theory,  $M$  and  $M^*$  should be approximate inverses of one another. Figure 7 shows the magnitude spectrum that results from the matrix product  $MM^*$  for the filters shown in Figures 1 and 2. Figures 8 and 9 are similar calculations for the filters of Figures 3 and 4 and Figures 5 and 6 respectively. If these filters were exact inverses of one another, these calculations would yield the identity matrix (which is a diagonal matrix with ones on the diagonal). It is apparent that these filters are not exact inverses but are very good approximate inverses.

## RESOLUTION SIMULATIONS

A resolution simulation is a numerical experiment designed to indicate the resolution capabilities of a particular seismic experiment. First-order effects can be assessed from the post-stack geometry and improvements that might be due to pre-stack migration are ignored. The simulation requires that an assumed reflectivity be forward modelled and then migrated. The resulting image is a prediction of the spatial resolution capabilities of a particular geometry.

Figure 10 shows a particular reflectivity that consists of a grid of impulses distributed over the aperture of the seismic section. Assuming a linear gradient of velocity with depth, Figure 11 shows the resulting exploding reflector model. The modelling was done with the  $v(z)$  f-k method described previously and requires that a zero-pad be attached, both laterally and vertically, to minimize Fourier wrap-around effects. The zero-pad has been retained in Figure 11 to illustrate a point about resolution. The velocity function was  $v(z) = 960 + .6z$  m/s .

The modelling response in Figure 11 shows that shallow impulses produce sharply peaked diffraction hyperbolae and deeper impulses have a more flattened response. If the zero-pads of Figure 11 were removed to restrict the response to the aperture of Figure 10, these diffraction responses would be truncated in ways that depends upon their position. A migration of this truncated result would produce resolution effects that vary throughout the aperture.

Alternatively, if the data of Figure 11 is migrated directly, using the  $v(z)$  f-k algorithm, the result is shown in Figure 12. As is apparent, all point diffractors are well-focussed regardless of their position. This is because the theory described above, when implemented with discrete Fourier transforms, assumes an infinite, periodic reflectivity and creates a similar response. In fact, the result in Figure 12, can be obtained without ever actually calculating the exploding reflector response. Instead, the spectrum of Figure 10 is simply multiplied by  $MM^*$  and inverse Fourier transformed.

To simulate the finite aperture and record length of real data, the data of Figure 11 can be truncated in both the horizontal and vertical dimensions and then migrated. The truncated dimensions were chosen to be those of the original reflectivity (Figure 10) and then the data were padded with zeros out to the dimensions of Figure 11. The  $v(z)$  f-k migration of the resulting data is shown in Figure 13. In comparison with Figure 12, it is immediately apparent that the size of focal points for each diffractor has become a function of the position of the diffractor. This result is not well modelled by the product  $MM^*$ . Instead, for this purpose  $MB_xB_tM^*$  is required where  $B_x$  is a Toeplitz matrix that applies a wavenumber convolution to achieve the aperture limit in  $x$  and  $B_t$  is a similar Toeplitz matrix that applies a frequency convolution for the record-length limit.

The  $v(z)$  simulation just described can be compared with a constant velocity simulation to illustrate the advantages of estimating acquisition parameters with the more realistic  $v(z)$  model. Figure 14 shows the forward model of the reflectivity of Figure 10 using a constant velocity of 2000 m/s. Again, a zero pad was used to minimize Fourier wrap-around. After truncation to the original dimensions the data were migrated at constant velocity and the result is shown in Figure 15.

The constant velocity simulation predicts optimal, symmetric focal points only in the precise center of the section. Minimal size is only found for the shallowest reflectivity. In contrast, the  $v(z)$  simulation shows small, symmetric focal points for a broad zone in the middle of the section. The simple explanation for this lies in the curved raypaths found in the  $v(z)$  world. Optimal focussing requires the imaging of a full set of raypaths covering all scattering angles from  $-90^\circ$  to  $90^\circ$ . In constant velocity, only straight rays are allowed and the  $\pm 90^\circ$  rays require infinite aperture to reach the surface. For the linear  $v(z)$  medium used in this simulation,  $\pm 90^\circ$  rays always reach the surface after finite traveltime and distance. This fact can be appreciated by a careful inspection of the diffraction hyperbolae in Figures 11 and 14. Many of the hyperbolae in Figure 11 can be seen to fade away in comparison with

Figure 14. This happens because the simulation did not include diving rays and so the fadeout corresponds to the limit of  $\pm 90^\circ$  rays.

Magnified views of comparable focal points from both the  $v(z)$  and constant-velocity simulations are enlightening. Figure 16 is a repeat of Figure 13 but with four boxes overlaid indicating the focal points to be examined. Figures 17, 18, 19, and 20 show enlargements of these focal points for both simulations. In each figure, the  $v(z)$  focal point is on the left while the constant-velocity focal point is on the right. In all cases, the  $v(z)$  focal point is substantially smaller, frequently by as much as a factor of 2.

These simulations illustrate the point that the design of seismic acquisition parameters using constant velocity theory to meet specific resolution requirements can lead to an overly expensive program. A  $v(z)$  simulation predicts much smaller resolution sizes than a constant velocity simulation because it accounts for raypath curvature.

## CONCLUSIONS

The  $v(z)$  f-k migration theory can be recast to give a WKBJ modelling theory. The modelling operator in the Fourier domain is a nonstationary filter that is the complex conjugate transpose (adjoint) of the migration operator. The product of these two operators is very nearly the unity operator. Post stack (exploding reflector) simulations show that, in the Fourier domain) the modelling operator is a lower triangular matrix while the migration operator is upper triangular. Both operators show power along hyperbolic paths, in the Fourier domain, that are determined by the instantaneous velocities. Models constructed using the  $v(z)$  f-k theory show much less effect from Fourier wrap-around than constant velocity models. When these models are truncated in aperture and record length and then migrated, they produce realistic resolution simulations. Such simulations for  $v(z)$  models predict dramatically better resolution than constant-velocity theory and will lead to acquisition designs with lowered costs.

## ACKNOWLEDGMENTS

I wish to thank the sponsors of the CREWES project for their support of this research.

## REFERENCES

- Aki, K., and Richards, P.G., 1980, Quantitative Seismology, Volume 1: W.H. Freeman and Co.  
Grant, F.S., and West, G.F., 1965, Interpretation theory in applied geophysics: McGraw-Hill, 584 pages.  
Lowenthal, D., Lu, L., Roberson, R., and Sherwood, J., 1976, The wave equation applied to migration: Geophysical Prospecting, **24**, 380-399.  
Margrave, G.F., 1997a, Zero offset seismic resolution theory for linear  $v(z)$ : CREWES Annual Research Report, **9**, chapter 1.

- Margrave, G.F., 1997b, Seismic acquisition parameter considerations for a linear velocity medium: 67<sup>th</sup> Annual SEG meeting, Dallas, Tx.
- Margrave, G.F., 1997, Nonstationary filtering: review and update: CREWES Annual Research Report, **9**, chapter 19.
- Margrave, G.F., 1998, Direct Fourier migration for vertical velocity variations: CREWES Annual Research Report, **10**, chapter 36.
- Margrave, G.F., and Ferguson, R.J., 1998, Nonstationary filters, pseudodifferential operators, and their inverses: CREWES Annual Research Report, **10**, chapter 26.
- Riley, K.F., Hobson, M.P., Bence, S.J., 1997, *Mathematical Methods for Physics and Engineering*: Cambridge University Press, ISBN 0521 55529 9.
- Stolt, R.H., 1978, Migration by Fourier Transform, *Geophysics*: **43**, 23-48.

### FIGURES

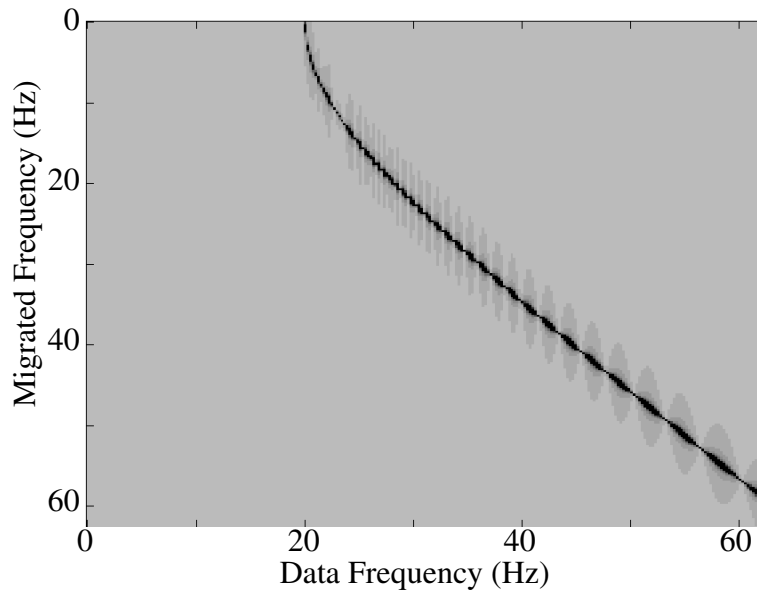


Figure 1. The Fourier domain migration filter,  $M(k_x, \xi, \omega)$ , is shown for a constant velocity of 2000 m/s.

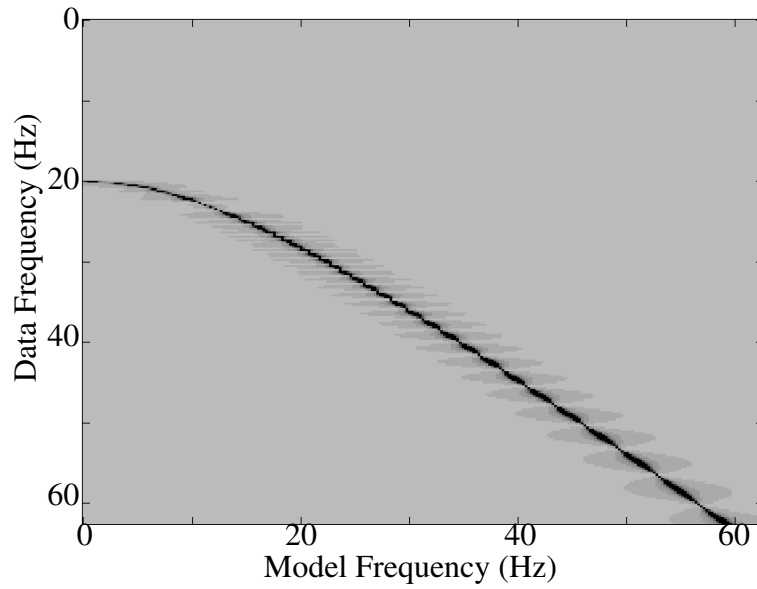


Figure 2. The Fourier domain modelling filter,  $M^*(k_x, \xi, \omega)$ , is shown for a constant velocity of 2000 m/s.

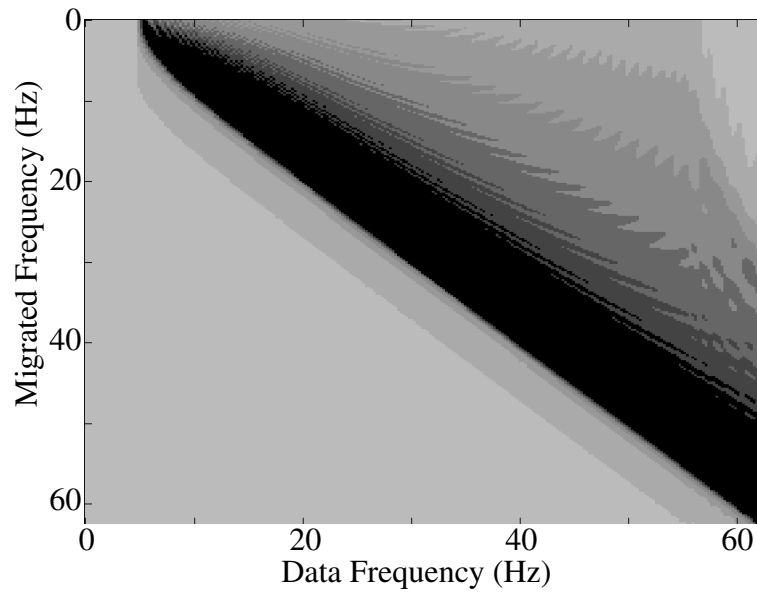


Figure 3. The Fourier domain migration filter,  $M(k_x, \xi, \omega)$ , is shown for  $v(z) = 1800 + .6z$  m/s.

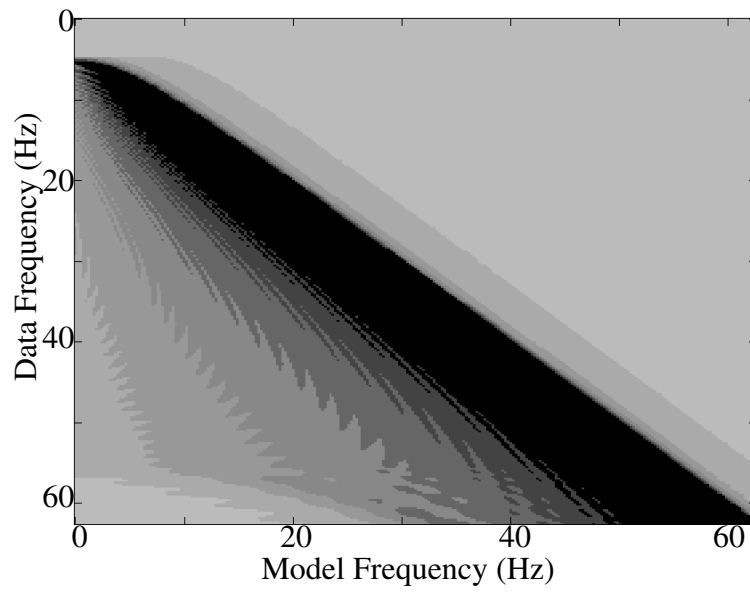


Figure 4. The Fourier domain modelling filter,  $M^*(k_x, \xi, \omega)$ , is shown for  $v(z) = 1800 + .6z$  m/s.

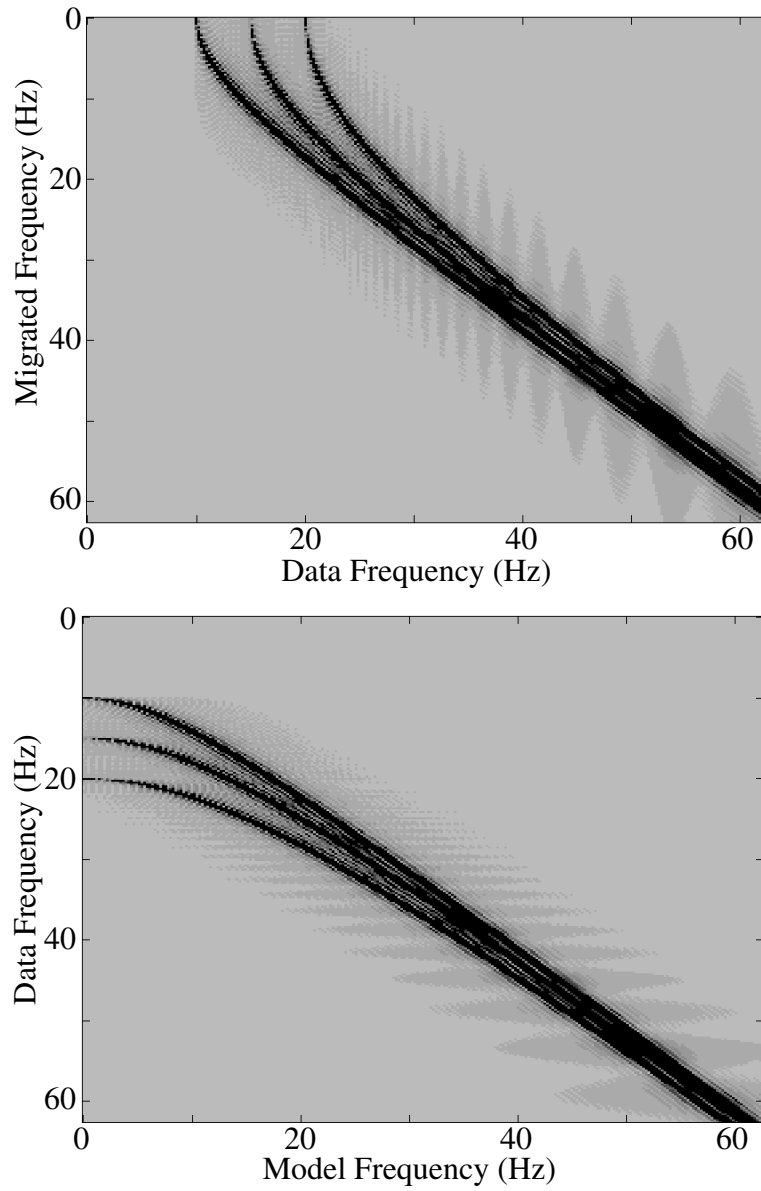


Figure 6. The Fourier domain modelling filter,  $M^*(k_x, \xi, \omega)$ , is shown for a three layer velocity function.

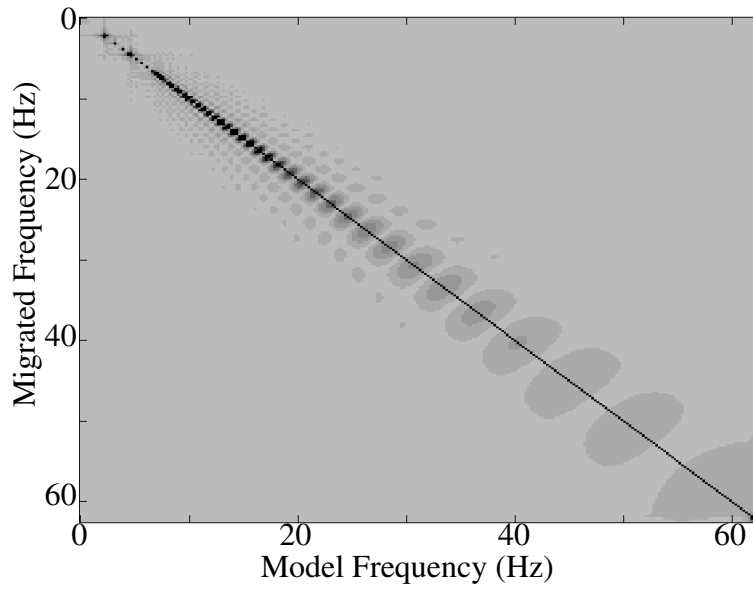


Figure 7. The product,  $MM^*$ , for the matrices of Figures 1 and 2. If  $M$  were a perfect inverse of  $M^*$ , then this would be a purely diagonal matrix.

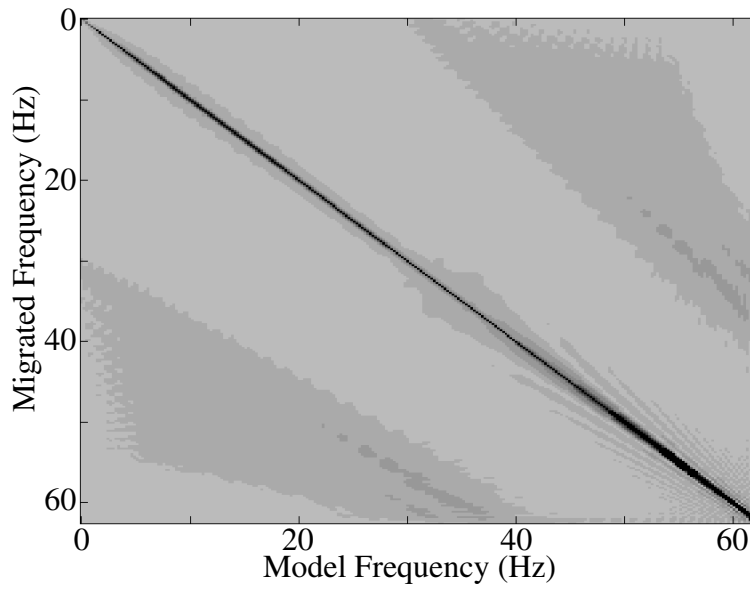


Figure 8. The product,  $MM^*$ , for the matrices of Figures 3 and 4. If  $M$  were a perfect inverse of  $M^*$ , then this would be a purely diagonal matrix.

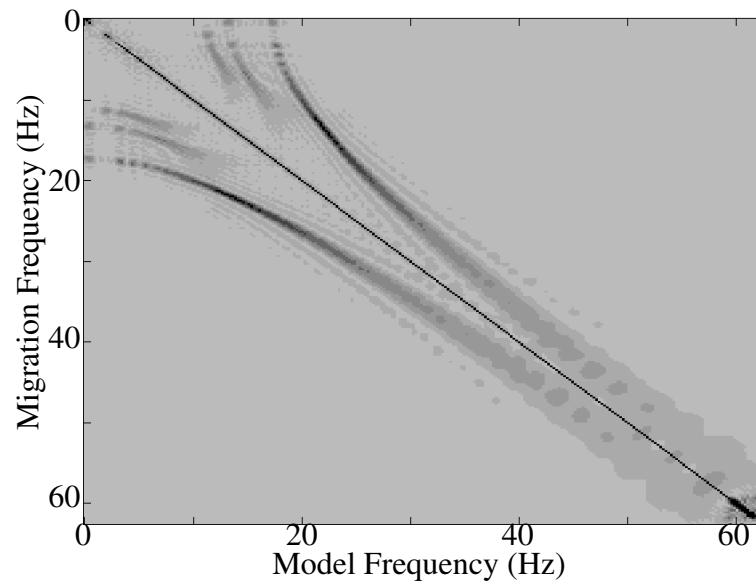


Figure 9. The product,  $MM^*$ , for the matrices of Figures 5 and 6. If  $M$  were a perfect inverse of  $M^*$ , then this would be a purely diagonal matrix.

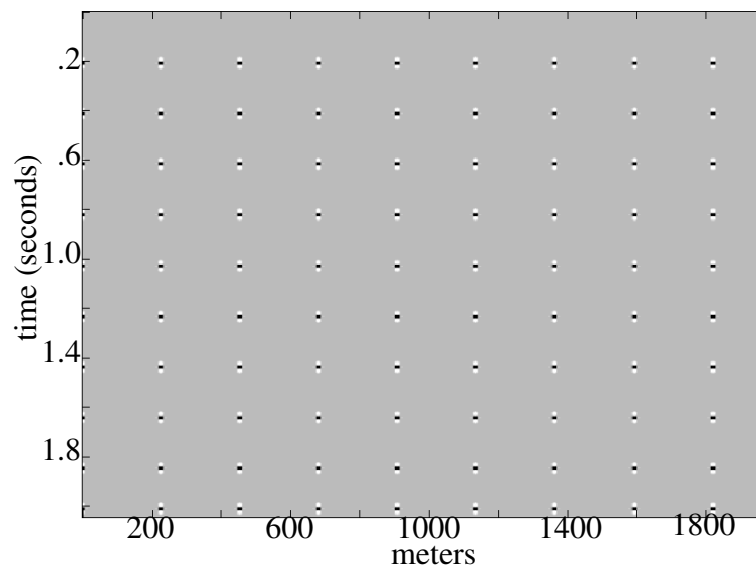


Figure 10. A grid to point scatterers to be used in modelling. The matrix is 512x512 samples and the point scatterers have been filtered (2D) to enlarge them for plotting. In the actual modelling, each scatterer was a single discrete sample of magnitude one.

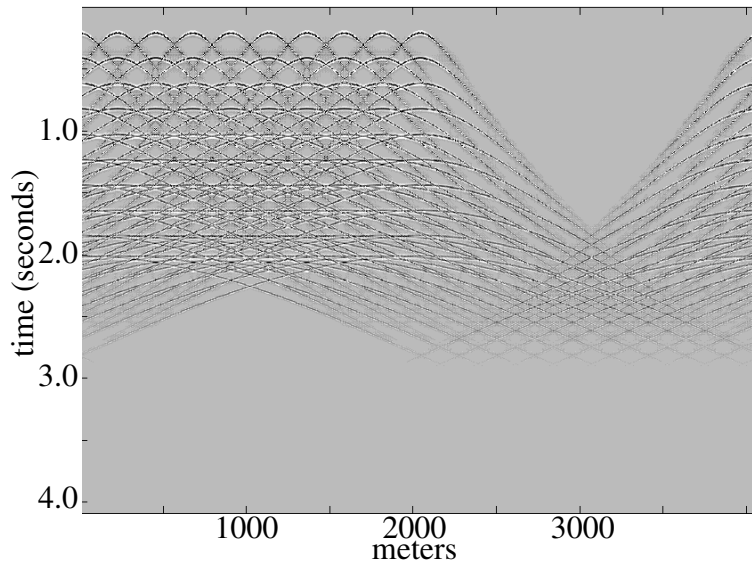


Figure 11. The modelling response of the  $v(z)$  f-k method for the reflectivity section of Figure 10. The velocity used was  $v(z) = 960 + .6z$  m/s . The spatial and temporal apertures of Figure 10 were doubled to control Fourier wrap-around.

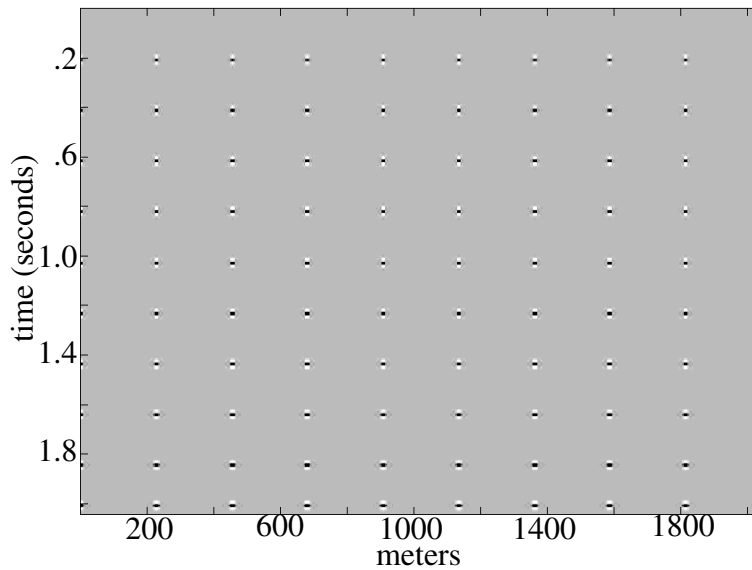


Figure 12. The  $v(z)$  f-k migration of the dataset in Figure 11 without any aperture or record length truncation before migration. The result, truncated temporally and spatially after migration, is a nearly perfect image of the reflectivity of Figure 10. This demonstrates that the operator product  $MM^*$  is nearly the identity operator.

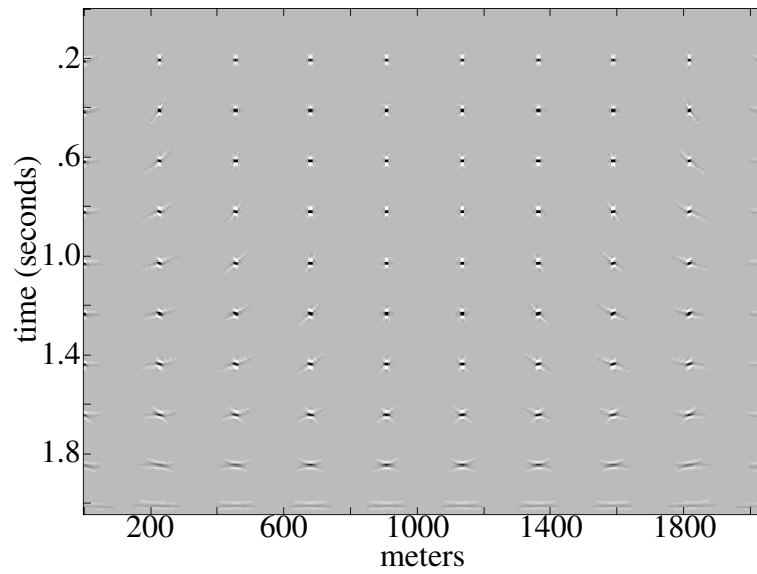


Figure 13. The  $v(z)$  f-k migration of the data of Figure 11 where the data were truncated to the aperture of Figure 10 (and then padded with zeros to the original size) before migration. Unlike Figure 12, the migrated result shows the expected geometric distortion due to finite aperture and record length.

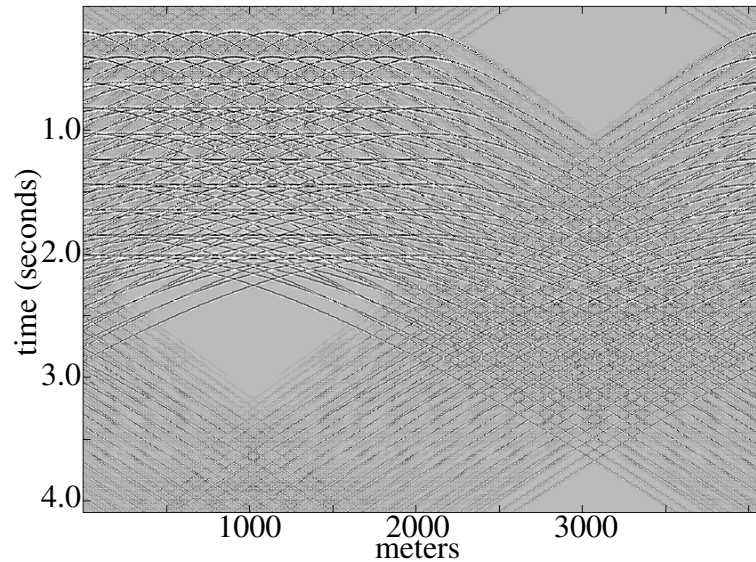


Figure 14. The constant-velocity modelling response (using the  $v(z)$  f-k algorithm) of the reflectivity of Figure 10. In comparison with Figure 11, there is a dramatic increase in Fourier wrap-around as well as a change in the shape of the diffraction response.

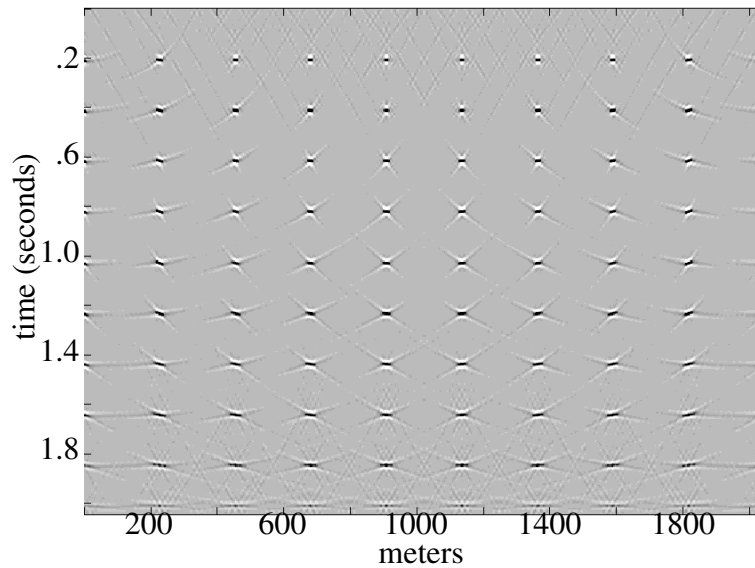


Figure 15. The constant-velocity migration (the  $v(z)$  f-k algorithm was used) of the dataset of Figure 14 where, before migration, the data was truncated temporally and spatially to the dimensions of Figure 10 (and then padded with zeros to the original size). The geometric distortion due to finite aperture and record length are much more severe in this case than in that of Figure 13.

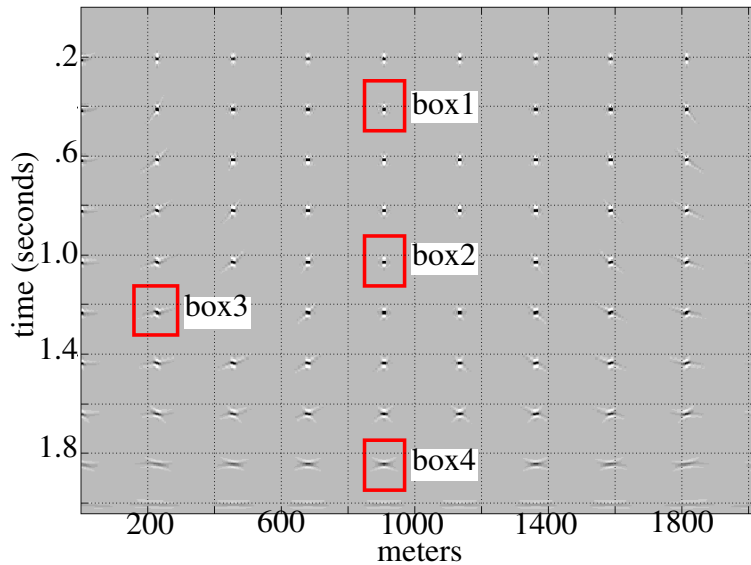


Figure 16. A repeat of Figure 13 with four analysis boxes shown whose contents are examined in Figures 17, 18, 19, 20.

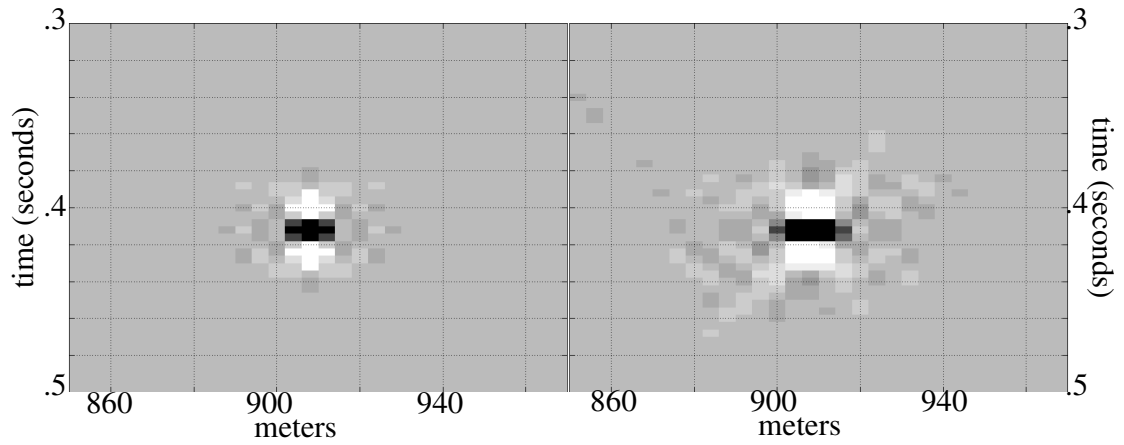


Figure 17. Zooms of the focal points within box1 (Figure 16) for the  $v(z)$  simulation of Figure 13 (left) and the constant-velocity simulation of Figure 15 (right).

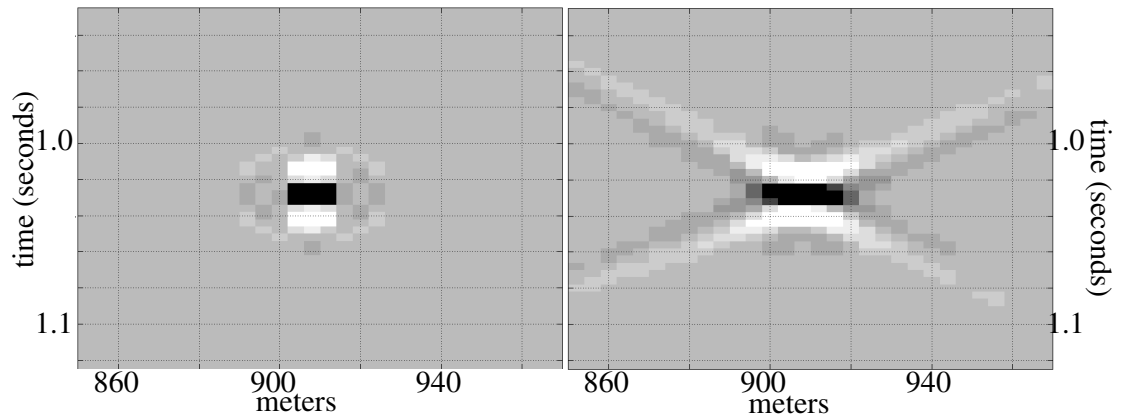


Figure 18. Zooms of the focal points within box2 (Figure 16) for the  $v(z)$  simulation of Figure 13 (left) and the constant-velocity simulation of Figure 15 (right).

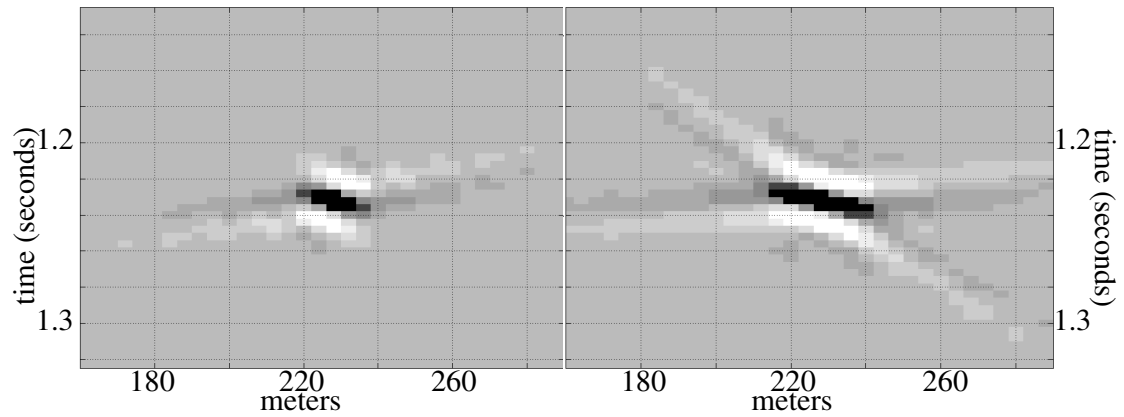


Figure 19. Zooms of the focal points within box3 (Figure 16) for the  $v(z)$  simulation of Figure 13 (left) and the constant-velocity simulation of Figure 15 (right).

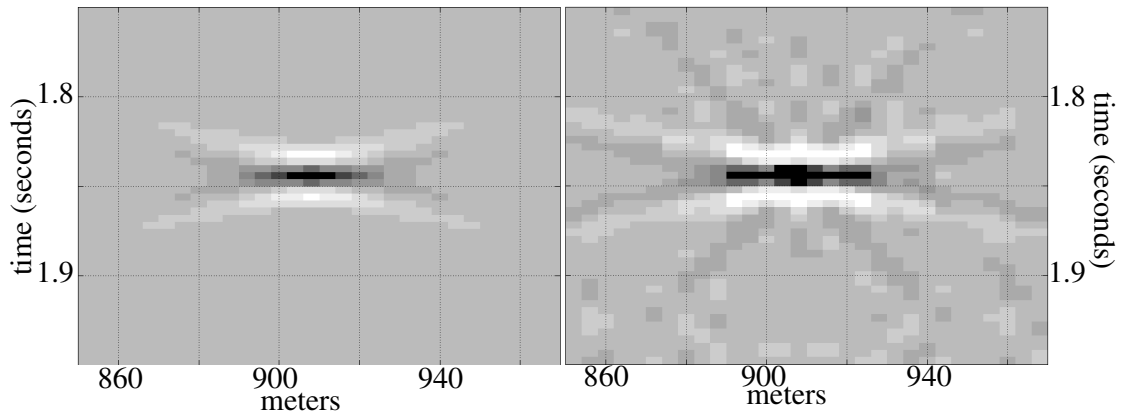


Figure 20. Zooms of the focal points within box4 (Figure 16) for the  $v(z)$  simulation of Figure 13 (left) and the constant-velocity simulation of Figure 15 (right).